Journal of Materials Chemistry A

Accepted Manuscript

ROYAL SOCIETY OF CHEMISTRY

www.rsc.org/materialsA

Journal Name

ARTICLE

Flexible-Wire Shaped All-Solid-State Supercapacitors Based on Facile Electropolymerization of Polythiophene with Ultra-High Energy Density

Received 00th January 20xx,
Accepted 00th January 20xx

DOI: 10.1039/x0xx00000x

www.rsc.org/

Rohan B. Ambade,[a] Swapnil B. Ambade,[a] Rahul R. Salunkhe,[b] Victor Malgras,[b] Sung-Ho Jin,[c] Yusuke Yamauchi *,[b] and Soo-Hyoung Lee*,[a]

Abstract

The new generation of miniaturized energy storage devices offers high energy and power densities and is compatible with flexible, portable, or wearable textile electronics which are currently in great demand. Here, we demonstrate the successful development of flexible, wire shaped (*f*-WS) all-solid-state symmetric supercapacitors (SCs) based on a facile electropolymerization of polythiophene (*e*-PTh) on titania (Ti) wire. The *f*-WS all-solid-state symmetric SCs, exhibiting high electrochemical performance, are fabricated by slightly intertwining two similar *e*-PTh electrodes to form both the cathode and anode which are then individually coated with a thin layer of H_2SO_4-PVA gel, acting both as the electrolyte and as a separator. The optimized devices (~1.5 cm long) based on *e*-PTh/Ti wire show a high capacitive performance (1357.31 mF g^{-1} or 71.84 mF cm^{-2}) and extremely high energy density (23.11 μWh cm^{-2}) at a power density of 90.44 μW cm^{-2} using a operational potential window of 1.8 V, which is beneficial for applications requiring high energy and power.The robust *f*-WS all-solid-state symmetric SCs also exhibit excellent mechanical flexibility with minimal change in capacitance upon bending at 360°. Furthermore, the SCs were implemented in the textile of a wearable/portable electronic device using conventional weaving method, thus demonstrating a high potential for next-generation wearable textile electronics applications.

Introduction

The rapid development of flexible, bendable, lightweight and portable electronics has gained vivid interests due to their versatile functionalities. Flexible devices can have various sizes and shapes and are lightweight and suitable for wearable textile applications.[1-9] Furthermore, miniaturizing flexible-wire shaped (*f*-WS) or fiber-based devices has gained increasing demand owing to the resulting superior characteristics such as flexibility, bendability, foldability, stretchability, lightweight and ability to be woven into textile fibers suitable for future portable and wearable electronics.[10-18] *f*-WS devices have recently shown great potential in various optoelectronic applications such as photovoltaics,[19-21] transistors,[22-23] sensors,[23] OLEDs,[24] photo generators,[25] as well as in batteries[26-27] and supercapacitors (SCs)[28-40] which can be woven into smart textiles.

Electrochemical cells, namely dye-sensitized solar cells (DSSCs), batteries and SCs have gained extensive attention for several decades as these devices efficiently convert or–store energy. Among various energy storage devices, SCs, also known as electrochemical capacitors or ultracapacitors, convert chemical energy into electrical energy. They have emerged as a bridge between batteries and traditional capacitors with a long lifespan, environmental benignity. In addition, their high performance along with being flexible, ultrathin, lightweight, foldable and wearable make them suitable candidates for the next-generation power devices.[41-45] SCs possess various advantages over batteries such as high energy storage, high power density, ultrafast charge-discharge (CD), and high operational lifetime. The energy storage mechanism can be described by two different models, 1) Carbon-based materials with a high surface area can store charges *via* electrostatic ion absorption in electrical double layer capacitors (EDLC). 2) Conducting polymer (CP) [45] and metal oxide[46-47] electrodes used in pseudocapacitors or redox supercapacitors[41-42] undergo fast and reversible faradic redox reaction, and achieve intercalations at the surface of the electrode. The performance of the EDLC is limited by the

[a] School of Semiconductor and Chemical Engineering, Chonbuk National University, 567 Baekje-daero, Jeonju, 54896, Republic of Korea. E-mail: shlee66@jbnu.ac.kr; Fax: +063-270-2306; Tel: +063-270-2435
[b] World Premier International (WPI) Research Centre for Materials Nanoarchitectonics (MANA), National Institute for Materials Science (NIMS), 1-1 Namiki, Tsukuba, Ibaraki 305-0044, Japan .Email: Yamauchi.Yusuke@nims.go.jp
[c] Department of Chemistry Education, Pusan National University, Busan, 46241, Republic of Korea

Electronic Supplementary Information (ESI) available: [Supplementary figures (Figure. S1-S13, Table S1-S2)]. See DOI: 10.1039/x0xx00000x

inherent low specific capacitance or non-faradic charge storage mechanism while pseudocapacitors show high capacitance behavior because of the high redox active capacitance and electrical conductivity. The use of carbon materials is limited to applications requiring high energy density devices due to their low capacitance. Metal oxides have a low conductivity, comparatively low surface area, and less stability and have thus limited applications in SCs. CPs, such as polypyrrole, polyaniline, polythiophene and their derivatives, have been widely explored as electrode materials for pseudocapacitors due to their salient features such as high redox activity, high electrical conductivity, low cost, ease of fabrication. The reversibility between redox states through doping/dedoping processes and the intrinsic flexible polymeric properties are fundamental requisites for portable flexible electronics.[45,48] The processing of CPs is typically achieved *via* multistep chemical or mechanical processing. Electropolymerization offers numerous advantages such as, absence of catalyst, low-cost, easy control over the thickness, ability to form adherent films on the electrodes,[49] and ease of synthesis. Thus, it is a promising technique to obtain binder-free CPs for high-performance SCs with minimum interfacial resistance and efficient electron transport.

Conventional planar SCs that use organic liquid electrolytes and wide potential window (4 V) suffer from a high cost of production and poor ionic conductivity. On the other hand, aqueous electrolytes have high ionic conductivity, are environmentally friendly, low cost, non flammable but also have a limited operating voltage (1.23 V). Furthermore, conventional planar SCs are rigid and heavy,[28] which limit their application in portable devices. Therefore, there is a great demand to develop lightweight and foldable *f*-WS or fiber-based all-solid-state SCs which can be employed in practical electronic textile applications.

Moreover, the low energy density of certain SCs is a major drawback which limits their utilization as an alternative to battery technology.[50-51] Efforts have been made to prepare new hybrid electrode materials to enhance the specific capacitance or energy density of SCs.[30, 52] Technically, the energy density can be enhanced by increasing either the specific capacitance (C_{sp}) or the operating cell voltage (V_{op}), as energy is proportional to CV_{op}^2. To date, most of the reports on *f*-WS SCs have mainly focused on increasing the C_{sp} with a low V_{op}, which limits the energy density of these electrodes. Thus, despite the improvement of C_{sp} in various *f*-WS SCs developed so far, they usually suffer from low energy density due to narrow working potential window.[28-40] As a result, fabricating an electrode with high energy density along with high specific power remains challenging. These objectives added to the ability of the device to be woven are important requirements to develop fast charging as well as intermediate specific energy solid-state *f*-WS SCs which can ultimately bridge the gap between batteries and SCs. The few studies that focus on increasing the energy density are majorly based on combining two or more positive and negative electrode materials such as composites of CNTs or graphene with transition metal oxide or CPs.[52] However, studies involving high energy density SCs (with high operating voltage) with electrode made of a single material are rare.

Herein, we have developed a facile strategy to design and engineer all-solid-state symmetric *f*-WS SCS based on an electropolymerized conducting polythiophene (*e*-PTh) on Ti wire. The SCS have high C_{sp} and ultra-high energy density and can be easily woven into textile fabrics. To the best of our knowledge, the unprecedented polythiophene-based solid-state *f*-WS SCs are being reported for the first time. Highly flexible all-solid-state SCs were prepared by slightly intertwining *e*-PTh/Ti wire electrodes using H_2SO_4-polyvinyl alcohol (PVA) gel as the electrolyte. The electrochemical studies show that as-fabricated device with both cathode and anode based on *f*-WS all-solid-state SSCs with *e*-PTh exhibited a C_{sp} of 1357.31 mF g^{-1} or 71.84 mF cm^{-2}. Due to excellent rate capability and an operating potential window of 1.8 V, an energy density as high as 23.11 μWh cm^{-2} has been obtained. Assembling the SCS using *e*-PTh with the same anode and cathode material is critical to simplify the fabrication process.

Experimental

Thiophene monomer, acetonitrile and tetrabutylammonium tetrafluoroborate (Bu_4NBF_4) were purchased from Sigma-Aldrich and were used as received without further purification. The Ti wire was obtained from Alfa Aesar.

Fabrication of *f*-WS all-solid-state SCS based on *e*-PTh/Ti wire

The electrochemical fabrication of *e*-PTh/Ti wire electrode was carried out through different polymerization cycles according to a method we reported previously.[53] Typically, the room-temperature electrochemical polymerization of a static mixture containing an optimized concentration of thiophene monomer and Bu_4NBF_4 in an acetonitrile medium was carried out at 25 mV s^{-1} on the cleaned surface of an extremely thin Ti wire. The meticulous control over the thickness was executed by varying the number of polymerizing cycles from 1 to 10. The obtained electrodes were naturally dried and coated using an electrolyte. The polymer gel electrolyte containing PVA and H_2SO_4 was prepared by mixing an aqueous solution of H_2SO_4 (1 M) with 1 g of PVA. The above mixture was heated at 90 ^oC under vigorous stirring to obtain a viscous and homogenous gel. Two as-prepared *e*-PTh/Ti wire (~1.5 cm) shaped electrodes were immersed in the H_2SO_4-PVA gel electrolyte for 1 min each, to ensure a superior polymer gel coating. The coating of gel electrolyte was carried out using a facile dip-coating method for 1 min each (optimized, see Figure S13), followed by drying at room temperature for ~4h. Afterward, the two electrodes were slightly intertwined and finally covered with a thin layer of gel electrolyte, followed by drying overnight, leading to the formation of the *f*-WS all-solid-state symmetric SCS. In addition to enabling a good stretchability, the gel electrolyte also acts as a separator and can prevent leakage and shorting in the SCs. It is to be noted that both *e*-PTh/Ti wires were uniformly coated with the gel electrolyte to avoid short-circuit between anode and cathode.

Electrochemical Measurements

All electrochemical measurements, including cyclic voltammetry (CV), galvanostatic charge/discharge (GCD) and electrochemical impendence spectroscopy (EIS), were performed using an Autolab-PGSTAT100 program operating on a potentiostat-galvanostat electrochemical workstation in the two-electrode configuration.

Characterizations

The morphology of the *f*-WS electrodes was studied using a Hitachi S-4700 Field emission scanning electron microscope (FE-SEM) coupled with energy-dispersive X-ray (EDX) spectroscopy. Transmission electron microscope (TEM) images were obtained with a JOEL JEM-2010 microscope operated at an acceleration voltage of 200 kV. N_2 adsorption/desorption isotherms of samples were measured on a BelSorp-mini adsorption-desorption analyser. The crystallographic information was obtained using X-ray diffraction (XRD) spectroscopy on a PANalytical X-pert diffractometer operating at 30kV and 20mA with a CuKα radiation (λ= 1.5405 Å) collected at a scan speed of 1^o min^{-1} using a step size of 0.04^o. The intensity distributions of the XRD data were fitted using JADE software from JADE Software Corporation, CA. The chemical bonding characteristics of the samples dispersed in standard potassium bromide (KBr) pellets were characterized by Fourier transform infrared spectroscopy (FT-IR, Shimadzu FT-IR-8700). Each FT-IR spectrum was collected after 32 scans at a resolution of 2 cm^{-1} from 4000 to 600 cm^{-1}. Raman spectroscopy and Raman mapping were carried out on an NT-MDT NTEGRA Spectra model using a 532 nm pumped solid state laser unit. X-ray photoelectron spectroscopy (XPS) measurements were performed using a Kratos Analytical Probe (A Shimadzu Group) system equipped with a monochromatic (Al) X-ray source (1486.6 eV). The calibration of binding energies was done by taking carbon (C 1s peak at 284.6 eV) as a reference. XPS measurements were also carried out with a twin anode and a charge neutralizer.

Results and discussion

The FE-SEM of the long flexible Ti wire can be observed in Figure 1a-b. The surface structure of the electrode (Ti wire) determines the adhesion, quality of coverage, charge-transfer characteristics, and morphology. It is known that the electropolymerization of thiophene on a given electrode is a surface-sensitive reaction.[54] The longitudinal view in Figure 1a shows a typical scaly Ti surface though quite clean and uniform across the entire length. The diameter estimated from the cross-sectional view in Figure 1b is 0.127 mm. Figure 1c shows the CV curves for the electropolymerization of thiophene on the Ti wire at a scan rate of 25 mV s^{-1}. The current response peak for thiophene monomer oxidation corresponding to *p*-doping is observed at 1.13 V in the first cycle. As the cycling progresses, the oxidation current peak increases and show a consistent shift to higher potentials. Recurrent cycling not only results in increasing the intensity of the oxidation current peak, but also in a systematic increase of the redox response

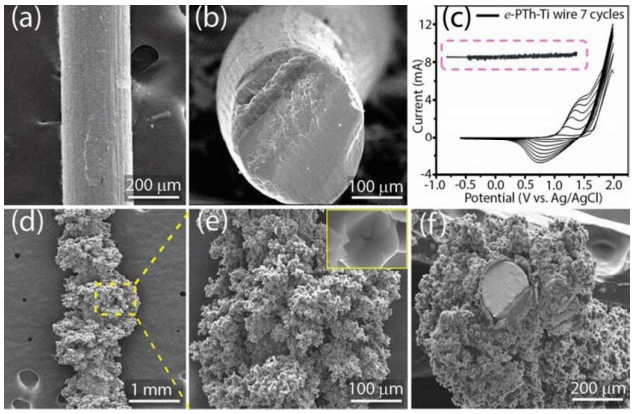

Figure 1. (a) FESEM images top view of bare Ti wire, (b) cross- section of bare Ti wire, (c) Cyclic voltammogram for electropolymerization of PTh/Ti at 7 cycles, (inset: digital photo image of the single *e*-PTh/Ti wire), (d-e) FESEM images of Ti-PTh at 7 cycles, (Inset in Figure 1e: high magnification FESEM image with scale bar 500 nm), (f) cross- section of Ti-PTh at 7 cycles.

of the *e*-PTh polymer, evidenced by the subsequent dedoping (reduction) process observed at around 0.8V for the first cycle.[55] During the cycling process, the sequential color change from reddish brown to deep blue is an indication of the doping and dedoping transitions, respectively. The current response for the first cycle is inferior to the rest of the polymer cycles. This suggests the occurrence of larger conductivity gradient between the highly conductive Ti metal and a fairly conducting PTh polymer. However, a more pronounced oxidation current is immediately observed at the second cycle, and continue to subsequently increase until the polymerization is terminated (after 7 cycles), indicating that, as the polymer grows, the conductivity rises.[55,56] The consistent augmentation in the oxidation current peak intensity suggests that each as-grown layer offers enough conductivity for the next layer to develop effectively. The CV curves also indicate that the polymer formed is quite stable, as can be deduced from the increasing resonance of the oligomeric structures formed during the early stages of electropolymerization. This is attributed to the presence of two lone non-bonding pairs of electrons in sulfur, from which only one pair is in the unhybridized *p*-orbital that overlaps with orbitals of carbon atoms in its structure.[57] To obtain polymer coatings of high homogeneity and greater adhesion, electropolymerization was carried out at a moderate scan rate of 25 mVs^{-1} (Figure S7).

After 7 polymerization cycles, the Ti wire is completely covered/wrapped by a highly porous *e*-PTh polymer, as can be seen in Figure 1d-f. According to BET analysis, the surface area was estimated to be 143 m^2 g^{-1} (Figure S8). As seen in Figure S8, the gas uptakes in the isotherms are gradually increased, meaning that the pore sizes are widely distributed. The micro-flake-like porous semi-spheres of *e*-PTh are clearly seen from the high magnification microscopic image given in the inset of Figure 1e. The semi-spheres of *e*-PTh become comparatively larger after each cycle (Figure S1-S2). The formation of semi-spheres in *e*-PTh is an indication of diffusion-controlled three-dimensional progressive nucleation and growth (3D-PNG).[58] 3D-PNG mechanisms involve a considerable number of nuclei and occur dominantly when electropolymerization is carried

out in a high potential window. Polymers grown *via* 3D-PNG are of great importance for optoelectronic applications, such as energy storage, since the formation of nuclei occurs at a lower rate and on a large number of active sites. Moreover, 3D nucleation constitutes oligomers with long chains compared to short chain oligomers formed during 2D growth. Long chain oligomers permit a greater delocalization of charge and eventually a higher conductivity. The uniformity of the coating can be assessed by locating the contrast between the Ti-wire (brighter region) and the *e*-PTh (darker region) on the cross-sectional view presented in Figure 1f. This uniform coating can be observed throughout the entire length of the electrode that was subject to electropolymerization. This can be expected from electrochemical polymerization, [56] where a polymer coating with a desired thickness can be obtained by simply manipulating the rate of polymerization. The various *e*-PTh microstructures obtained at different polymerization cycles are shown in Figure S1-S2. It is observed that the polymer growth is exponential with increasing the cycling rate. A striking feature arising from controlling the degree of cycling is the ability to tune the porosity of the polymer. High magnification FE-SEM images of different polymerizing cycles presented in Figure S1-S2 clearly show that the porosity starts to diminish at higher rates of polymerization. For example, after 10 cycles (Figure S2j1-j3), highly rigid and non-porous *e*-PTh layers can be seen. Such a compact layer suffers from a serious barrier hindering the diffusion of electrolyte ions, ultimately resulting in a lower electrochemical activity. From the cross-sectional image in Figure 1e, it is important to point out that there is a small non-bonded region at the interface separation between the *e*-PTh polymer and the metallic Ti-wire. However, further investigations of the inner layers do not show the presence of any fracture or cracks, indicating a good adherence. The presence of few non-bonded regions does not hinder the overall activity since the electrode (Ti wire) doesn't actively participate in the electrochemical charge storage.

The porous nature of *e*-PTh, evidenced on the TEM images

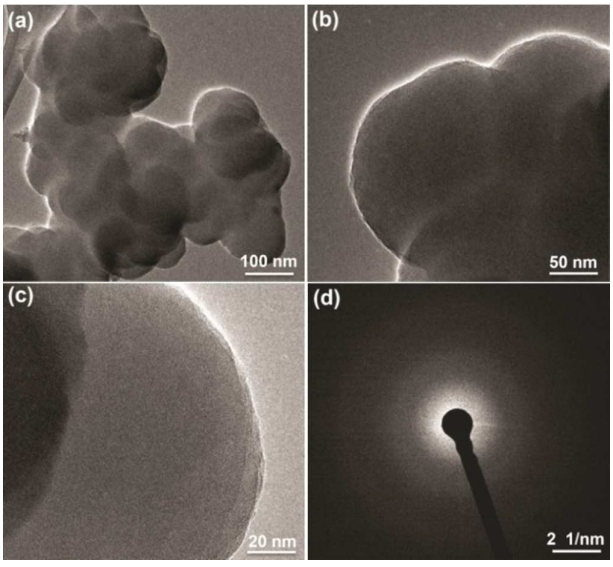

Figure 2. (a-c) TEM images and (d) SAED pattern of *e*-PTh/Ti wire 7 cycles.

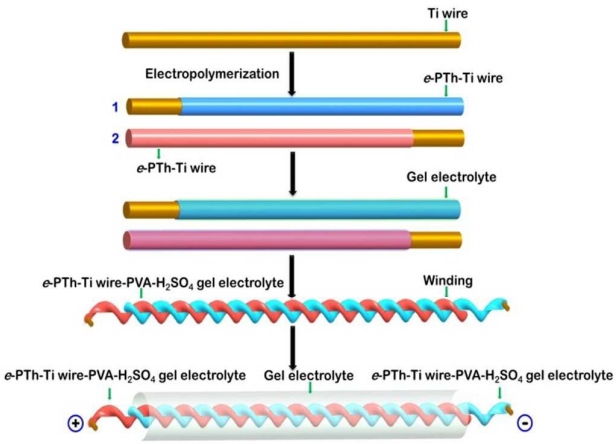

Figure 3. Schematic illustrations of the fabrication process of an *f*-WS all-solid-state symmetric SC based on *e*-PTh/Ti wire.

displayed in Figure 2a-c, is essential for an efficient electrolyte diffusion and ionic movement. Figure 2a indicates that the individual spherical *e*-PTh structures typically form an interconnected network while the magnified images (Figure2b-c) show that the antipodes of the spheres are ~200 nm apart. The corresponding selected area electron diffraction (SAED) pattern displayed in Figure 2d indicates the amorphous nature of the porous *e*-PTh. The coated Ti-wires were assembled to fabricate a *f*-WS all-solid-state symmetric SCs. In this configuration, the role of the *e*-PTh and the Ti-wire was that of an active electrode and a current collector, respectively.

A representative scheme of the *f*-WS all-solid-state symmetric SCs (with the fabrication of *e*-PTh on Ti-wire) is illustrated in Figure 3. Two similar electrodes were obtained by electropolymerizing PTh (*e*-PTh) on Ti-wires to form the cathode and anode, followed by individually coating each of them with a thin layer of H_2SO_4-PVA gel electrolyte that also acts as a separator. To achieve a good infiltration of the gel electrolyte, the samples coated with the gel were first dried for an adequate time before being slightly intertwined together to achieve high-quality compact assembly. This intertwined system was finally coated with gel electrolyte for a second time to ensure an intimate contact between the electrolyte and the electrodes.

FE-SEM images of a single electrode coated with the gel electrolyte are shown in Figure 4a-f. For a controlled polymerization of 7 cycles, PVA wraps the *e*-PTh-coated Ti-wire neatly (Figure 4a). A high magnification image in Figure 4b shows that the gel electrolyte covers *e*-PTh completely. Typical fibrils of PVA are seen in Figure 4c. An intercalated H_2SO_4-PVA matrix can be observe on the wire polymerized for 10 cycles, as shown in Figure 4d-f. It is clear that even for a thicker polymer coating, the gel electrolyte holds and protects the polymer without letting any of the layers mechanically peel off or fracture. It is noteworthy that the H_2SO_4-PVA coverage on each *e*-PTh/Ti-wire sample was over 99%. This is attributed to the amphiphilic nature of PVA that possesses a water contact angle (WCA) of ~72°.[59] Moreover, according to previous reports, [60] electropolymerized polythiophenes exhibit a WCA of c.a. 81°. This suggests that PVA and *e*-PTh can form an

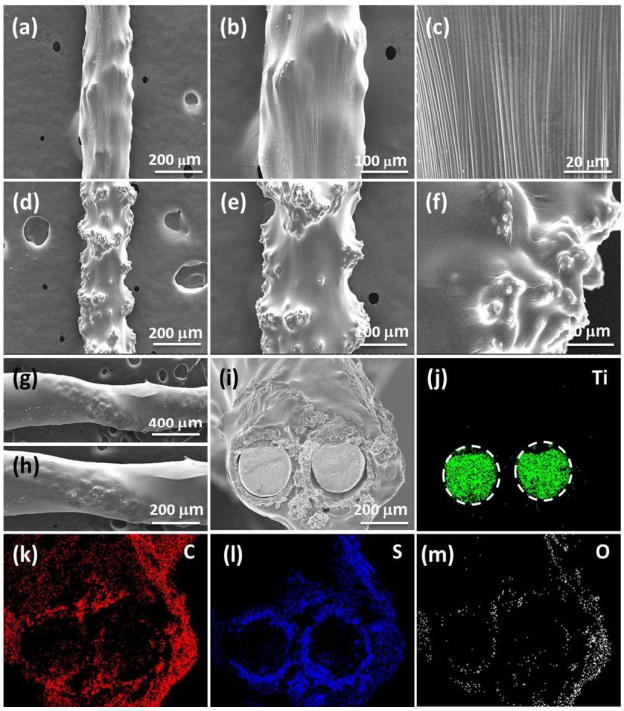

Figure 4. FE-SEM images of coaxial fiber (a-c) *e*-PTh/Ti wire at 7 cycles with PVA-H_2SO_4 gel electrolyte, (d-f) *e*-PTh/Ti wire at 10 cycles with PVA-H_2SO_4 gel electrolyte, (g-h) slightly interwoven *e*-PTh/Ti wire at 7 cycles both wires with the gel electrolyte, (i) cross-section of slightly interwoven *e*-PTh/Ti wire at 7 cycles both wires with the gel electrolyte, (j-m) elemental mapping for slightly interwoven *e*-PTh/Ti wire at 7 cycles both wires with the gel electrolyte.

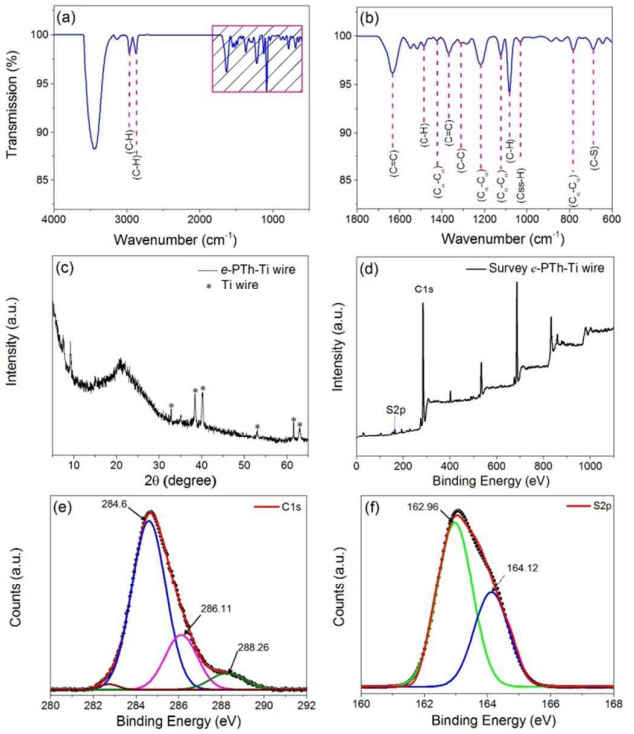

Figure 5. (a-b) FT-IR spectra, (c) XRD, (d) XPS survey, (e) C1s XPS spectra and (d) S 2p XPS spectra of *e*-PTh/Ti wire for 7 cycles.

excellent interfacial synergy. The samples were too small to perform any WCA measurements, however, this effect is apparent from the fact that PVA could not cover any of the regions which were not pre-coated with *e*-PTh, owing to the extremely high surface energy of Ti metal. The intertwined solid-state assembly of the two *e*-PTh electrodes wrapped in the H_2SO_4-PVA gel electrolyte is shown in Figure 4 g-h. It is seen that the *e*-PTh/Ti wire surface is uniform and smooth due to the gel electrolyte coating. The cross-sectional FE-SEM image (Figure 4i) shows that the two intertwined *e*-PTh/Ti-wire electrodes are well separated by ~40 μm electrolyte. Such thick electrolyte coating should provide an efficient separation between the two electrodes and circumvent any possible electrical shorting. The elemental distribution of the intertwined solid-state supercapacitor assembly (i.e., C, S, O, Ti), was acquired through EDX mapping of the cross-section (Figure 4j-m). As C and S (from *e*-PTh) constitute the major fractions compared to O (from H_2SO_4-PVA), the presence of a considerable amount of thiophene on the Ti wire is clearly evidenced. The EDX spectrum is illustrated in Figure S4. The highly distributed nature of *e*-PTh on the Ti wires is critical to achieve excellent charge storage capability.

To quantitatively confirm the formation of *e*-PTh, FT-IR transmission spectra were acquired as shown in Figure 5a-b. The peak at 3450 cm^{-1} can be assigned to O-H stretching vibrations due to the hygroscopic nature of the dopant in PTh polymer. The peaks between 3133 and 2800 cm^{-1} were attributed to C-H stretching vibrations.[61] The signature peak region for PTh is observed between 1800-600 cm^{-1}. FT-IR peaks, assigned in detail in Table S1, show conclusively the presence of PTh obtained by electropolymerization.[62] The characteristic peaks at 1428, 1112 and 785 cm^{-1} clearly suggest that the *e*-PTh is a dominant C_α-C_α position linkage or 2, 5 disubstituted thiophene ring, and eventually suggest that *e*-PTh/Ti wire has a considerable conducting nature, as the C_α–C_α conjunction is known to have good conductivity.[63] The vibration band at 1222 cm^{-1} is associated with the interring stretching of C_α-$C_{\alpha'}$ linkage along the PTh backbone.[53, 64] The FT-IR spectra of all the electrodes reveal that the absorption peak of the C_α–C_α conjunction of PTh observed at 785 cm^{-1} (Figure S9) is incredibly intense after 7 cycles as compared to less polymerization cycles. This clearly suggests that the *e*-PTh–Ti electrode is the most electroactive after 7 cycles. When the thiophene monomer is electropolymerized for 7 cycles, surfaces with well-ordered structures impose certain boundary constraints to the participating monomers, avoiding possible random polymerization of thiophene and simultaneously maintaining the parent symmetry and C_α–C_α coupling reaction. The controlled ordering of PTh units eventually prevent independent nucleation and growth of the ordering regions as the polymer continues to build-up on existing polymerization sites. In contrast, after long polymerization processes (above 8 cycles), there is limited or perhaps no control over the growth and ordering of the polymer because of the subsequent mutual impingement of numerous PTh units. These impingements give rise to a myriad of defects with distorted chain linkages. Such defects in a given chain can as well introduce distortions in adjacent chains and thus modify their electronic distribution which can favour the formation of

further linkage and stacking errors. This is suggestive of a sharp decrease of conductivity and electrochemical properties in case of high deposition of polymer.

The crystalline nature of *e*-PTh/Ti wire was confirmed using XRD performed between 5 and 60° (Figure 5c). The peaks at 5.2°, 7.5° and 9.2° are assigned to the lamellar planes formed due to the side-by-side stacking of chains.[65] The typical halo-like broad peak centered at 21° associated with the intermolecular π–π stacking is due to the amorphously formed PTh main chain.[63a] The Ti metal substrate peaks are clearly identified in Figure 5c. Furthermore, *e*-PTh was also confirmed and characterized by XPS. The wide energy survey spectrum (Figure 5d) exhibits the expected elemental compositions such as carbon (C) and sulfur (S). To elucidate the chemical bonding, high-resolution XPS spectra were investigated as shown in Figure 5e-f. The C1s XPS spectrum can be deconvoluted into three peaks centered at 284.6, 286.11 and 288.26 eV. The lower binding energy peak centered at 284.6 eV is attributed to the α and β aromatic carbons of the polymeric backbone of *e*-PTh.[66] The higher binding energy peaks at 286.11 and 288.26 eV are assigned to the C=C-S and C=O groups due to the over-oxidation state during the electropolymerization of thiophene, which is in good agreement with the FT-IR data. [67] The S2p core-level spectrum (Figure 4f) of the *e*-PTh can be deconvoluted into two spin-orbit-split doublets from the thiophene sulfur atom, *viz* $S2p_{3/2}$ and $S2p_{1/2}$ peaks centered at 162.96 eV and 164.12 eV, respectively.[68]

The polymeric fingerprint of *e*-PTh was also identified using Raman and Raman mapping as shown in Figure 6. The peaks centred at 695.37 cm^{-1} and 1045.19 are assigned to C-S-C coplanar vibrations and C-H bending mode of the thiophene ring, respectively. The Raman maps of the spectrum integrated between 695.37 cm^{-1} and 1045.19 are shown in Figure 6b-c.[68] The active regions show the presence of *e*-PTh. The band associated with the vibration of the C_α-$C_{\alpha'}$ linkage between adjacent thiophene rings is observed at 1220 cm^{-1}.[69] Raman mapping of the spectrum integrated between 1214 and 1247 cm^{-1} is shown in Figure 6d. The intense peak at 1457.89 cm^{-1} is assigned to the symmetric stretching mode of the aromatic C=C bond ring for PTh in the neutral state.[68] The Raman mapping of the spectrum integrated between 1430 and 1485cm^{-1} is shown in Figure 6e. The peak at 2848 cm^{-1} is associated with C-H stretching, and the corresponding mapping is shown in Figure 6f.

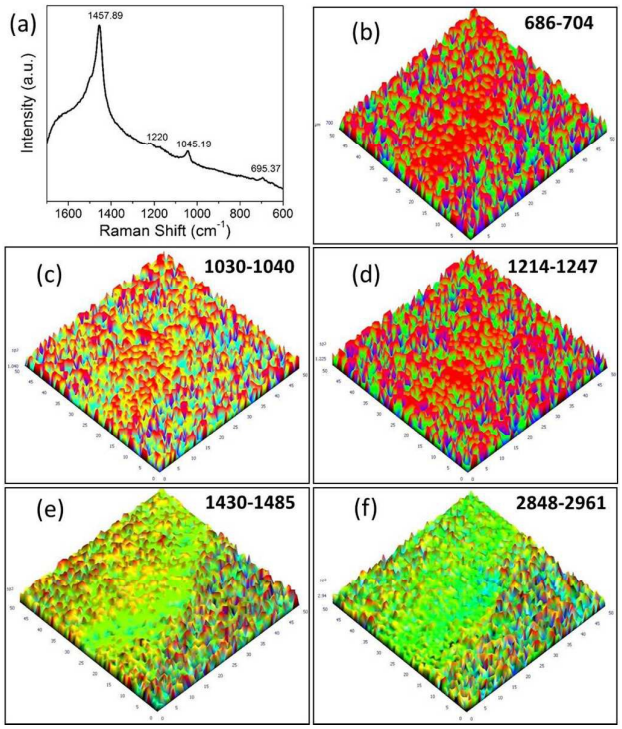

Figure 6. (a) Raman spectra and (b-f) 3D image of Raman mapping of *e*-PTh, brighter areas represent areas of a polymer.

Electrochemical Characterization and Performance of *f*-WS all-solid-state symmetric SCs based on *e*-PTh/Ti wire

The electrochemical performance of the *f*-WS all-solid-state symmetric SCs based on *e*-PTh/Ti wire was evaluated by CV, GCD and EIS using a two-electrode configuration. The *e*-PTh was polymerized under different conditions from 1 to 10 polymerization cycles on a Ti wire at the optimized scan rate of 25 mV s^{-1}. To study the electroactivity after various numbers of polymerization cycles, the CV curves are illustrated in Figure 7a-b. For all cycles, the *e*-PTh redox characteristic peaks are observed between -0.5 V and +0.5 V. As the polymerization cycles increase from 1 to 7, the maximum current of the redox peaks increase as well. By further increasing the number of polymerization cycles from 7 to 10, redox properties were found to be reduced, suggesting that the pseudo-capacitive properties of the *f*-WS solid-state symmetric SCs are optimal when the *e*-PTh/Ti wire undergoes 7 polymerization cycles. The corresponding CV curves of different polymerization conditions (1 to 10 cycles) at different scan rates from 5 to 100 mVs^{-1} are presented in Figure S10. It is clear that all *e*-PTh/Ti wire *f*-WS solid-state symmetric SCs with various

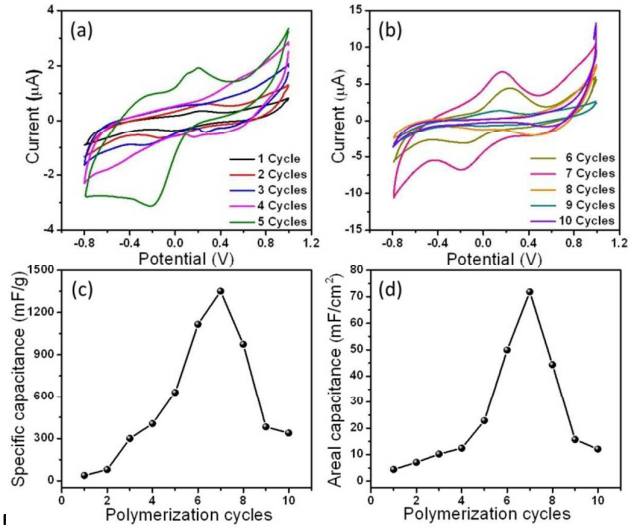

different numbers of polymerization cycles of *e*-PTh/Ti wire at 25 mVs^{-1}.

polymerization conditions show redox property, showcasing the excellent pseudocapacitor behavior of such structure. It is also evident that the C_{sp} increases with increasing the number of cycles from 1 to 7, and further drops for the following 8th, 9th and 10th cycles (Figure 7c-d). The C_{sp} of the SCs based on *e*-PTh/Ti wire, scanned at a gradual sweep rate of 5mV s^{-1}, is enhanced from 38.08 to 1351.31 mF g^{-1} as the number of polymerization cycles increased from 1 to 7 and then decreased to 339.11 mF g^{-1} by further increasing up to 10 cycles (Figure S11). The enhancement in C_{sp} with increasing the number of polymerization cycles (from 1 to 7) is accredited to the excellent pseudocapacitance offered by *e*-PTh, which eventually results from the uniform and amorphous morphology of *e*-PTh on Ti wire. Moreover, after 10 cycles, a rigid and brittle *e*-PTh with low flexibility is developed (Figure S2j). Such a rigid structure significantly hinders efficient transport and diffusion of ions, which then eventually decrease the performance of the SCs.[70] In addition, increased rigidity and decreased flexibility for high polymerization cycles (from cycles 8-10) put serious limitations to their use in flexible, wearable electronic applications. Thus, we choose 7 polymerization cycles of *e*-PTh/Ti wire as an optimum condition. It is also noteworthy that, unlike *e*-PTh, the Ti wire substrate contributed minimally to the overall capacitance.

To evaluate the performance of the optimized polymerization condition of the *f*-WS all-solid-state symmetric SC based on *e*-PTh/Ti wire with 7 polymerization cycles, CV measurements were performed in a two-electrode

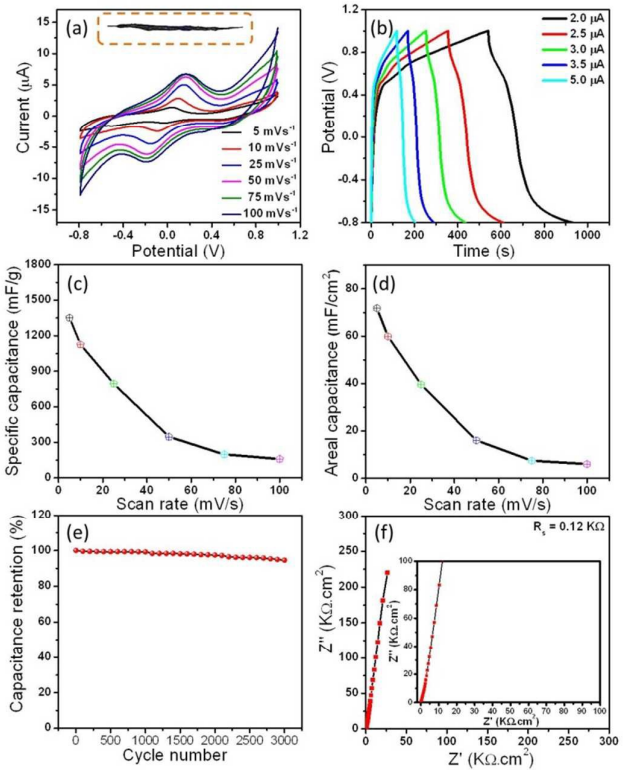

Figure 8. (a) CV curves at different sweep rates (inset is a digital photo of the device), (b) charge-discharge at different current densities, (c) specific capacitance (d) areal capacitance (e) cycling stability and (f) electrochemical impedance spectroscopy of *e*-PTh/Ti wire for 7 cycles wire based all-solid-state supercapacitors.

configuration at various scan rates ranging from 5 to 100 mVs^{-1} with a maximum cell voltage window of 1.8 V (-0.8 V to 1 V) (Figure 8). It is observed from Figure 8a that increasing the scan rate lead the currents and the area under the CV curves to increase as well, indicating that the *e*-PTh electrodes have a excellent capacitive behavior. Importantly, the redox peaks are retained even at higher scan rates. From the CV curves, the areal capacitances calculated (following equations S1 and S2) for scan rates of 5 mV s^{-1} and 100 mV s^{-1} are 71.84 mF cm^{-2} and 5.98 mF cm^{-2}, respectively. The capacitance measured as a function of scan rate is presented in Figure 8c. A substantial drop in capacitance at high scan rates suggests a slow diffusion of ions.

To further evaluate the electrochemical performance of the *f*-WS all-solid-state symmetric SC based on *e*-PTh/Ti wire with 7 cycles, GCD measurements were carried out in the voltage range from -0.8 to 1 V at a current of 2 μA. The linear and symmetrical charge-discharge curves indicate an excellent supercapacitor behavior. The SC based on *e*-PTh/Ti wire with 7 cycles show a much longer discharging time (Figure 8b) than for the other polymerization cycles. The areal capacitance at different current densities (Figure 8b) was calculated from the GCD curves using equations S4 and S5. The areal capacitance of *e*-PTh/Ti wire for 7 cycles at a current density of 2 μA is calculated to be as high as 55.71 mF cm^{-2}, which is in good agreement with the CV results (Figure 8a). It is to be noted that the areal capacitance of bare Ti wire is minimal. From the GCD curves, the results clearly show that the SC based on 7 cycles exhibit excellent rate capability.

The cycling stability of an electrode is one of the most important requirements for practical implementation in energy storage devices.[30] To investigate the cyclic stability of the *f*-WS all-solid-state symmetric SC based on *e*-PTh/Ti wire with 7 cycles, GCD was performed for 3000 cycles, as illustrated in Figure 8e. There is no obvious change in the capacitance even after 3000 cycles and still retains 97% of its initial performance, clearly showcasing the excellent cycling stability of the SC. The limited structural damage of *f*-WS *e*-PTh/Ti wire during the long GCD process due to the gel electrolyte helps to achieve superior cycling stability.

Furthermore, the excellent electrochemical performance of *f*-WS all-solid-state symmetric SC based on the *e*-PTh/Ti wire with 7 cycles can be explained by its small intrinsic resistance. The charge transport and ion diffusion are studied using EIS measurements. Figure 8f illustrates the Nyquist plots of the EIS spectra with a frequency ranging from 10 kHz to 0.01 Hz. The equivalent series resistance (ESR) of the *f*-WS electrode obtained from the *x*-intercept of the Nyquist plot is 0.12 KΩ. The straight line nearly parallel to the imaginary axis (Figure 8f, inset), showcases the excellent capacitive behavior of the *e*-PTh/Ti wire electrode.[28-34]

To test the flexibility and bendability of *f*-WS electrodes, CV measurements at 100 mV s^{-1} are carried out for the straight (planar) and bent (360°) states as shown in Figure 9a. The areas under the CV curves from the straight and bended samples are almost identical, and no significant capacitance drop can be observed, clearly suggesting that the the *e*-PTh/Ti

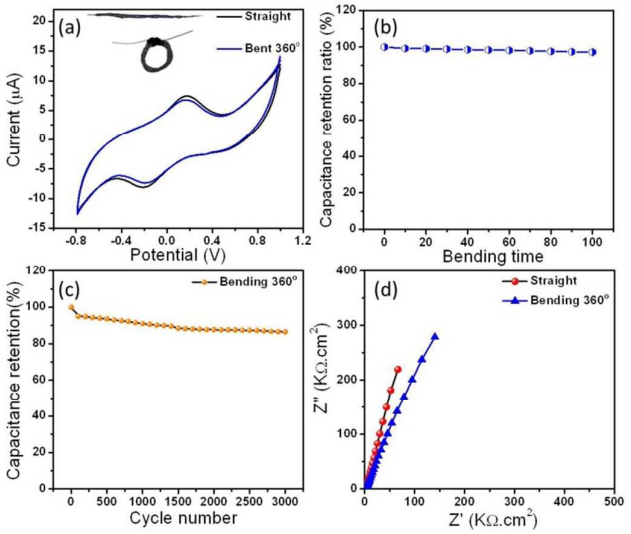

Figure 9. (a) CV curves with flexibility test for straight and bending angle (360°) of *e*-PTh/Ti wire for 7 cycles at 100 mV/s (Inset: demonstrate the bending angle of the *e*-PTh/Ti wire *f*-WS solid state SCs), (b) capacitance stability in bending state for 100 cycles, (c) cycling stability after bending at 360° undergoing 3000 cycles and (d) EIS in straight and bending state.

wire coated with the polymer gel electrolyte is highly flexible in nature. The capacitance was maintained even at high mechanical bending (360°), and it is mainly due to the superior adhesion of *e*-PTh on the Ti wire (current collector), which was prepared by simple electropolymerization method. This also proves that the internal structure of the *f*-WS electrode is well maintained and does not undergo any physical damage, even after harsh bending at 360°. Thus, the excellent mechanical stability and flexibility are clearly evidenced in our *e*-PTh/Ti *f*-WS SCs, which are crucial parameters for practical applications in portable and wearable electronics. Also, minimal change in the capacitance, stability and EIS can be observed in the *f*-WS all-solid-state symmetric SC based on *e*-PTh/Ti wire with 7 cycles even after bending at 360° for 100 times, proving its excellent flexibility, electrochemical and mechanical stability (illustrated in Figure 9a-d). Moreover, no mechanical fractures or damage occurred before and after bending.[71-72]

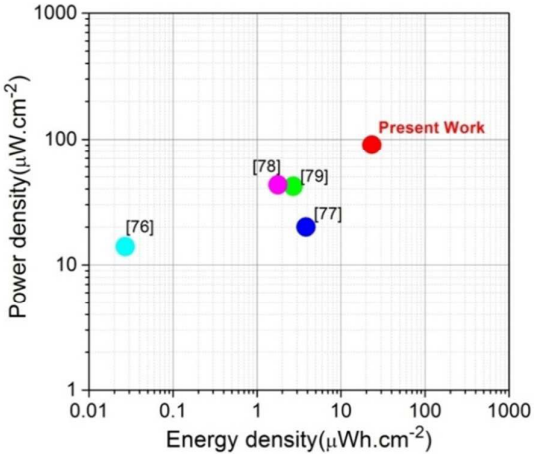

Figure 10. Ragone plots of *f*-WS *e*-PTh/Ti wire SCs (red) compared with other supercapacitor devices.

The energy density (E) and power density (P) are important parameters used to illustrate the electrochemical performance of SCs. E and P is derived from GCD curves following equations S6 and S7. The Ragone plot (energy density *vs.* power density) measured in the 1.8 V potential window (-0.8 V to 1 V) of the *f*-WS all-solid-state symmetric SC based on *e*-PTh/Ti wire 7 cycles is shown in Figure 10. A maximum energy density of 23.26 μWhcm^{-2} and power density of 90.44 μWcm^{-2} is obtained. Compared with the literature data based on *f*-WS (Table S2 & Figure 10), the energy density of our SCs is much higher. These high energy and power densities of *f*-WS electrode are due to the wide potential window of 1.8 V, high ion permeability through porous morphology, and conducting nature of *e*-PTh, which provides ionic and electron pathways.

As compared to conventional SCs, the unique feature of *f*-WS SCs is to be flexible, wearable, which can be woven/knitted into the textiles and its potential to be easily incorporated to form integrated multifunctional devices. The *f*-WS all-solid-state symmetric SCs based on *e*-PTh/Ti wire are further employed to explore their application in flexible and wearable electronic device, which can be woven into the textile by simple conventional weaving method. Figure 11 illustrates that the *e*-PTh/Ti wire (~1.5 cm each) with different polymerization conditions (1 to 10 cycles) were easily woven into the glove. The top and bottom sides of woven *f*-WS electrodes are shown in Figure 11a-b and Figure 11c, respectively. This clearly indicates that the woven electrodes prepared from simple *e*-PTh are flexible and can be integrated into portable electronic textiles, which is expected to fulfill the requirements of flexible wearable textile electronics.[29, 73-75]

The superior enhancement in the performance of our *f*-WS *e*-PTh/Ti wire SCs can be attributed to the following factors. First, the optimal content of deposited polymer along with the high conducting nature of *e*-PTh/Ti wire and its porous morphology provides sufficient electrochemically active sites for an efficient reversible redox reactions. The porous nature of *e*-PTh can promote access to more electrochemical sites for

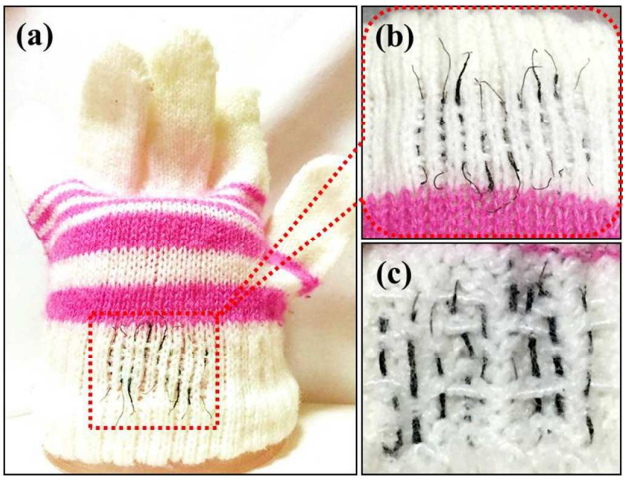

Figure 11. (a-b) *f*-WS *e*-PTh/Ti wire weaving into a glove for textile application (10 wire based solid state supercapacitor was ~1.5 cm long), and (c) bottom side of the woven *f*-WS *e*-PTh/Ti wire.

the GCD. Second, the thick morphology of the *e*-PTh/Ti wire keeps the two electrodes apart, avoiding the occurrence of short-circuits. This morphology provides more open spaces accessible by the gel electrolyte, thus providing an excellent GCD and ultimately improving the stability of the *f*-WS all-solid-state symmetric SCs based on the *e*-PTh/Ti wire. Third, the low ESR in the *e*-PTh/Ti wire electrodes also helps in improving the performance of the *f*-WS all-solid-state symmetric SCs. Fourth and most importantly, the large operating potential window of 1.8 V significantly contributes to achieve a high energy and power densities. We envisage that these exciting features, along with the ability to develop free-standing conducting polymers directly on the current collector (wire-shaped substrate) with control over thickness and porosity provide a complementary pathway for the design of environmentally stable wearable supercapacitors.

Conclusions

In summary, a high-performance flexible wire shaped all-solid-state supercapacitor based on a facile electropolymerization of polythiophene on a Ti wire is successfully demonstrated. The optimum electropolymerization of 7 cycles resulted in a high capacitance of 1357.31 mF g^{-1} or 71.84 mF cm^{-2}, an excellent rate capability and an outstanding cycling stability over 3000 cycles. Furthermore, a wide operating potential window of 1.8 V provided an extremely high energy density of 23.11 $\mu Wh.cm^{-2}$ at a power density of 90.44 $mWcm^{-2}$. The robust and *f*-WS SC is shown to be perfectly suitable for electronic applications in wearable/portable textiles.

Acknowledgements

This research was supported by the Pioneer Research Centre Program through the National Research Foundation (NRF) of Korea funded by the Ministry of Science, ICT & Future Planning (NRF-2013M3C1A3065528). This work was also supported by grant fund from the NRF (2011-0028320) by the Ministry of Science, ICT & Future Planning of Korea.

Notes and references

1 Z. Liu, J. Xu, D. Chen and G. Shen, *Chem. Soc. Rev*., 2015, **44**, 161–192.
2 T. Chen and L. Dai, *J. Mater. Chem. A*, 2014, **2**, 10756–10775.
3 M. F. El-Kady, V. Strong, S. Dubin and R. B. Kaner, *Science*, 2012, **335**, 1326–1330.
4 L. Wang, X. Feng, L. Ren, Q. Piao, J. Zhong, Y. Wang, H. Li, Y. Chen and B. Wang, *J. Am. Chem. Soc.*, 2015, **137**, 4920–4923.
5 Y-Z. Zhang, Y. Wang, T. Cheng, W-Y. Lai, H. Pang and W. Huang, *Chem. Soc. Rev*., 2015, **44**, 5181–5199.
6 H. Nishide and K. Oyaizu, *Science,* 2008, **319**, 737-738.
7 Y-H. Lee, J-S. Kim, J. Noh, I. Lee, H. J. Kim, S. Choi, J. Seo, S. Jeon, T-S. Kim, J-Y. Lee and J. W. Choi, *Nano Lett.,* 2013, **13**, 5753−5761.
8 K. Cherenack, C. Zysset, T. Kinkeldei, N. Münzenrieder and G. Tröster, *Adv. Mater.,* 2010, **22**, 5178–5182.
9 L. Hu, M. Pasta, F. L. Mantia, L. Cui, S. Jeong, H. D. Deshazer, J. W. Choi, S. M. Han and Y. Cui, *Nano Lett*., 2010, **10**, 708–714.
10 Z. Cai, L. Li, J. Ren, L. Qiu, H. Lin and H. Peng, *J. Mater. Chem. A*, 2013, **1**, 258–261.
11 C. Choi, J. A. Lee, A. Y. Choi, Y. T. Kim, X. Lepró, M. D. Lima, R. H. Baughman and S. J. Kim, *Adv. Mater*., 2014, **26**, 2059–2065.
12 V. T. Le, H. Kim, A. Ghosh, J. Kim, J. Chang, Q. A. Vu, D. T. Pham, J-H. Lee, S-W. Kim and Y. H. Lee, *ACS Nano*, 2013, **7**, 5940–5947.
13 Z. Zhang, X. Chen, P. Chen, G. Guan, L. Qiu, H. Lin, Z. Yang, W. Bai, Y. Luo and H. Peng, *Adv. Mater*., 2014, **26**, 466–470.
14 T. Chen, L. Qiu, Z. Yang, Z. Cai, J. Ren, H. Li, H. Lin, X.Sun and H. Peng, *Angew. Chem. Int. Ed*., 2012, **51**, 11977–11980.
15 Y. Fu, H. Wu, S. Ye, X. Cai, X. Yu, S. Hou, H. Kafafy and D. Zou, *Energy Environ. Sci*., 2013, **6**, 805–812.
16 L. Li, Z. Wu, S. Yuan and X-B. Zhang, *Energy Environ. Sci*., 2014, **7**, 2101–2122.
17 H. Peng, DOI 10.1007/978-3-662-45744-3.
18 K. Jost, G. Dion and Y. Gogotsi, *J. Mater. Chem. A*, 2014, **2**, 10776–10787.
19 T. Chen, L. Qiu, Z. Yang and H. Peng, *Chem. Soc. Rev.,* 2013, **42**, 5031–5041.
20 T. Chen, L. Qiu, Z. Cai, F. Gong, Z. Yang, Z. Wang and H. Peng, *Nano Lett*., **2012**, *12*, 2568–2572.
21 D. Liu, M. Zhao, Y. Li, Z. Bian, L. Zhang, Y. Shang, X. Xia, S. Zhang, D. Yun, Z. Liu, A. Cao and C. Huang, *ACS Nano*, 2012, **6**, 11027–11034.
22 S. Nam, J. Jang, J-J. Park, S. W. Kim, C. E. Park and J. M. Kim, *ACS Appl. Mater. Interfaces,* 2012, **4**, 6−10.
23 W. Zeng, L. Shu, Q. Li, S. Chen, F. Wang and X-M. Tao, *Adv. Mater.,* 2014, **26**, 5310–5336.
24 B. O'Connor, K. H. An, Y. Zhao, K. P. Pipe and M. Shtein, *Adv. Mater.,* 2007, **19**, 3897–3900.
25 J. Zhong, Y. Zhang, Q. Zhong, Q. Hu, B. Hu, Z. L. Wang and J. Zhou, *ACS Nano*, 2014, **8**, 6273–6280.
26 J. Ren, L. Li, C. Chen, X. Chen, Z. Cai , L. Qiu, Y. Wang, X. Zhu and H. Peng, *Adv. Mater.,* 2013, **25**, 1155–1159.
27 M. Peng, K. Yan, H. Hu, D. Shen, W. Song and D. Zou, *J. Mater. Chem. C*, 2015, **3**, 2157–2165.
28 D. Yu, Q. Qian, L. Wei, W. Jiang, K. Goh, J. Wei, J. Zhang and Y. Chen, *Chem. Soc. Rev.,* 2015, **44**, 647–662.
29 K. Jost, D. Stenger, C. R. Perez, J. K. McDonough, K. Lian, Y. Gogotsi and G. Dion, *Energy Environ. Sci*., 2013, **6**, 2698–2705.
30 X. Dong, Z. Guo, Y. Song, M. Hou, J. Wang, Y. Wang and Y. Xia, *Adv. Funct. Mater.,* 2014, **24**, 3405–3412.
31 J. A. Lee, M. K. Shin, S. H. Kim, H. U. Cho, G. M. Spinks, G. G. Wallace, M. D. Lima, X. Lepro´, M. E. Kozlov, R. H. Baughman and S. J. Kim, *Nat. Commun.*, **2013**, *4*, 1970.
32 X. Wang, K. Jiang and G. Shen, *Materials Today*, 2015, **18**, 265–272.
33 Q. Wang, X. Wang, J. Xu, X. Ouyang, X. Hou, D. Chen, R. Wang and G. Shen, *Nano Energy*, 2014, **8**, 44–51.
34 Z. Yang, J. Deng, X. Chen, J. Ren and H. Peng, *Angew. Chem. Int. Ed.,* 2013, **52**, 13453–13457.
35 S. Pan, H. Lin, J. Deng, P. Chen, X. Chen, Z. Yang and H. Peng, *Adv. Energy Mater.,* **2014**, 1401438.
36 Y. Shang, C. Wang, X. He, J. Li, Q. Peng, E. Shi, R. Wang, S. Du, A. Cao and Y. Li, *Nano Energy*, 2015, **12**, 401–409.
37 J. Tao, N. Liu, W. Ma, L. Ding, L. Li, J. Su and Y. Gao, *Sci Rep.* 2013, **3**, 2286.
38 X. Wang, B. Liu, R. Liu, Q. Wang, X. Hou, D. Chen, R. Wang and G. Shen, *Angew. Chem., Int. Ed.*, 2014, **126**, 1880–1884.
39 G. Sun, J. Liu, X. Zhang, X. Wang, H. Li, Y. Yu, W. Huang, H. Zhang and P. Chen, *Angew. Chem. Int. Ed.,* 2014, **53**, 12576–12580.

40 Y. Huang, H. Hu, Y. Huang, M. Zhu, W. Meng, C, Liu, Z, Pei, C, Hao, Z. Wang and C. Zhi, *ACS Nano*, 2015, **9**, 4766–4775.
41 M. Winter and R. J. Brodd, *Chem. Rev*. 2004, **104**, 4245−4269.
42 B. E. Conway, Electrochemical Supercapacitor, Scientific Fundamentals and Technological Applications, Kluwer Academic/Plenum, New York, 1999.
43 P. Simon and Y. Gogosti, *Nat. Mater.,* 2008, **7**, 845–854.
44 G. Wang, L. Zhang and J. Zhang, *Chem. Soc. Rev*., 2012, **41**, 797–828.
45 G. A. Snook, P. Kao and A. S. Best, *J. Power Sources,* 2011, **196**, 1–12.
46 R. R. Salunkhe, J. Tang, Y. Kamachi, T. Nakato, J. H. Kim and Y. Yamauchi, *ACS Nano*, 2015, **6**, 6288–6296.
47 R. R. Salunkhe, J. Lin, V. Malgras, S. Xue Dou, J. H. Kim and Y. Yamauchi, *Nano Energy*, 2015, **11**, 211–218.
48 B. Anothumakkool, R. Soni, S. N. Bhange and S. Kurungot, *Energy Environ*. *Sci*., 2015, **8**, 1339–1347.
49 S. Alkan, C. A. Cutler and J. R. Reynolds, *Adv. Funct. Mater*., 2003, **13**, 331–336.
50 Z. Dai, C. Peng, J. H. Chae, K. C. Ng and G. Z. Chen, *Sci Rep.*, 2015, **5**, 9854.
51 J. Yan, Q. Wang, T. Wei and Z. Fan, *Adv. Energy Mater.,* 2014, **4**, 1300816.
52 Z. Zhang, F. Xiao and S. Wang, *J. Mater. Chem. A*, 2015, **3**, 11215–11223.
53 R. B. Ambade, S. B. Ambade, N. K. Shrestha, Y-C. Nah, S-H. Han, W. Lee and S-H. Lee, *Chem. Commun.*, 2013, **49**, 2308–2310.
54 M. F. Suarez-Herrera and J. M. Feliu, *J. Phys. Chem. B* 2009, **113**, 1899–1905.
55 X. Chen and O. Inganas, *J. Phys. Chem.* 1996, **100**, 15202–15206.
56 J. Heinze, B. A. Frontana-Uribe and S. Ludwigs, *Chem. Rev*., 2010, **110**, 4724–4771.
57 G. C. Arteaga M. A. del Valle, M. Antilén, F. R. Díaz, M. A. Gacitúa, P. P. Zamora, J. C. Bernède, L. Cattin and G. Louarn, *Int. J. Electrochem. Sci*., 2012, **7**, 7840–7854.
58 D. Kowalski and P. Schmuki, *ChemPhysChem* 2012, **13**, 3790–3793.
59 L. Feng, Y. Song, J. Zhai, B. Liu, J. Xu, L. Jiang and D. Zhu, *Angew. Chem*. *Int. Ed.,* 2003, **115**, 824–826.
60 R. J. Waltman, A. F. Diaz and J. Bargon, *J. Phys. Chem.*, 1984, **88**, 4343-4346.
61 Y. Wang, W. Chu, S. Wang, Z. Li, Y. Zeng, S. Yan and Y. Sun, *ACS Appl. Mater. Interfaces*, 2014, **6**, 20197–20204.
62 H. Goktas, F. G. Ince, A. Iscan, I. Yildiz, M. Kurt and I. Kaya, *Synthetic Met.*, 2009, **159**, 2001–2008.
63 (a) F. Wu, J. Chen, R. Chen, S. Wu, L. Li, S. Chen and T. Zhao, *J. Phys. Chem. C* 2011, **115**, 6057–6063, (b) X. Li and Y. Li, *J. Appl. Polym. Sci.,* 2003, **9**, 940–946.
64 X. Wang, G. Shi and Y. Liang, *Electrochem Commun.*, 1999, **1**, 536–539.
65 S. Nagamatsu, K. Kaneto, R. Azumi, M. Matsumoto, Y. Yoshida and K. Yase, *J. Phys. Chem. B* 2005, **109**, 9374–9378.
66 Tourillion, G. In Handbook of Conducting polymers; Skoteim, T. A., Ed.; Marcel Dekker: New York, 1986; p 296.
67 J. Heeg, C. Kramer, M. Wolter, S. Michaelis, W. Plieth and W.-J. Fischer, *Applied Surface Science*, 2001, **180**, 36–41.
68 M. R. Karim, K. T. Lim, C. J. Lee and M. S. Lee, *Synthe. Met.*, 2007, **157**, 1008–1012.
69 Q-T. Vu, M. Pavlik, N. Hebestreit, U. Rammelt, W. Plieth and J. Pfleger, *React Funct Polym.*, 2005, **65**, 69–77.
70 J. Tao, N. Liu, W. Ma, L. Ding, L. Li, J. Su and Y. Gao, *Sci Rep.* **2013**, 3, 2286.
71 W. Xiong, X. Hu, X. Wu, Y. Zeng, B. Wang, G. He and Z. Zhu, *J. Mater. Chem. A*, 2015, **3**, 17209–17216.
72 W. Zhou, K. Zhou, X. Liu, R. Hu, H. Liu and S. Chen, *J. Mater. Chem. A*, 2014, **2**, 7250–7255.
73 K. Jost, D. P. Durkin, L. M. Haverhals, E. K. Brown, M. Langenstein, H. C. D. Long, P. C. Trulove, Y. Gogotsi and G. Dion, *Adv. Energy Mater.,* 2014, **5**, 1401286.
74 L. Liu, Y. Yu, C. Yan, K. Li and Z. Zheng, *Nat. Commun.*, 2015, **6**, 7260.
75 Y. Meng, Y. Zhao, C. Hu, H. Cheng, Y. Hu, Z. Zhang, G. Shi and L. Qu, *Adv. Mater.,* 2013, **25**, 2326–2331.
76 J. Bae, M.K. Song, Y.J. Park, J.M. Kim, M. Liu and Z. L. Wang, *Angew. Chem. Int. Ed.,* 2011, **50**, 1683–1687.
77 L. Kou, T. Huang, B. Zheng, Y. Han, X. Zhao, K. Gopalsamy, H. Sun and C. Gao, *Nat. Commun.*, 2014, **5**, 3754.
78 J. Ren, W. Bai, G. Guan, Y. Zhang and H. Peng, *Adv. Mater.,* 2013, **25**, 5965–5970.
79 Y. Fu, X. Cai, H. Wu, Z. Lv, S. Hou, M. Peng, X. Yu and D. Zou, *Adv. Mater*., 2012, **42**, 5713–5718.

Graphical Abstract

Flexible-Wire Shaped All Solid-State Supercapacitors based on Facile Electropolymerization of Polythiophene with Ultra-high Energy Density

Rohan B. Ambade,[a] Swapnil B. Ambade,[a] Rahul R. Salunkhe,[b] Victor Malgras,[b] Sung-Ho Jin,[c] Yusuke Yamauchi*,[b] and Soo-Hyoung Lee*,[a]

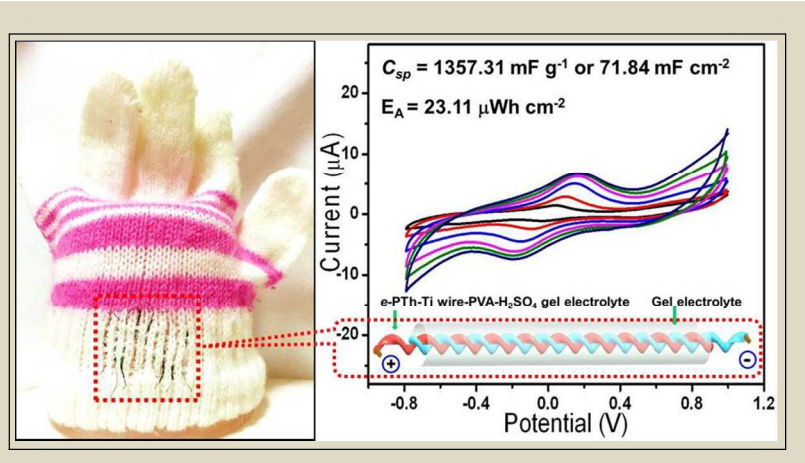

The flexible-wire shaped all-solid-state-supercapacitors developed by electropolymerization of polythiophene, show high capacitive performance of 1357.3 mF g^{-1} or 71.84 mF cm^{-2} and ultra- high energy density of 23.11 μWh cm^{-2} at a power density of 90.44 μW cm^{-2} using a wide operational potential window of 1.8 V.